# Thermodynamic Analysis on Wetting Behavior of Hierarchical Structured Superhydrophobic Surfaces

H. H. Liu, H. Y. Zhang, and W. Li*

Faculty of Material and Photoelectronic Physics, Key Laboratory of Low Dimensional Materials & Application Technology (Ministry of Education), Xiangtan University, Hunan, Xiangtan 411105, People's Republic of China, and State Key Laboratory of Electrical Insulation and Power Equipment, and State Key Laboratory for Manufacturing Systems Engineering, Xi'an Jiaotong University, People's Republic of China

ABSTRACT: Superhydrophobicity of biological surfaces has recently been studied intensively with the aim to design artificial surfaces. It has been revealed that nearly all of the superhydrophobic surfaces consist of the intrinsic hierarchical structures. However, the role of such structures has not been completely understood. In this study, different scales of hierarchical structures have been thermodynamically analyzed using a 2-D model. In particular, the free energy (FE) and free energy barrier (FEB) for the composite wetting states are calculated, and the effects of

relative pillar height (h_r) and relative pillar width (a_r) on contact angle (CA) and contact angle hysteresis (CAH) have been investigated in detail. The results show that if the geometrical parameter ratio is the same (e.g., $a{:}b{:}h = 2{:}2{:}1$), the equilibrium CA for the composite of the three-, dual-, and single- scale roughness structures is 159.8°, 151.1°, and 138.6°, respectively. Furthermore, the nano- to microstructures of such surfaces can split a large FEB into many small ones and hence can decrease FEB; in particular, a hierarchical geometrical structure can lead to a hierarchical "FEB structure" (e.g., for a dual-scale roughness geometrical structure, there is also a dual-scale FEB structure). This is especially important for a droplet to overcome the large FEBs to reach a stable superhydrophobic state, which can lead to an improved self-cleaning property. Moreover, for extremely small droplets, the secondary or third structure (i.e., submicrostructure or nanostructure) can play a dominant role in resisting the droplets into troughs, so that a composite state can be always thermodynamically favorable for such a hierarchical structured system.
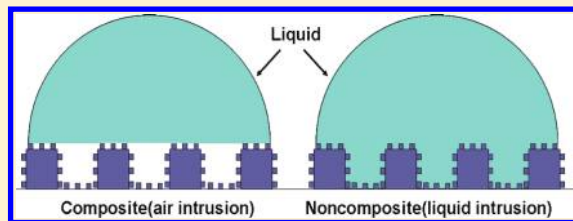
1. INTRODUCTION

Fractal, which means irregular and broken object, was first introduced into Science by Mandelbrot[1−3] in the 1970s to characterize complex figures and processes. A fractal is a shape made of parts similar to the whole in some way. Mandelbrot[3] shows that fractal geometry can imitate nature. A typical example is lotus leaf. The fractal structure of the leaf shows not only excellent water-repellent or self-cleaning property but also stable and good mechanical properties.[4] The ability of these structures to make water bead off completely and thereby wash off contamination very effectively has been termed the "Lotus effect", which shows numerous promising applications such as self-cleaning window glasses, paints, textiles, solar panels, antifouling, and microchannels. Recently, many studies[5−7] have widely investigated natural fractal structures to understand the mechanisms for the unique superhydrophobic, self-cleaning, low adhesion, and drag reduction behavior, aiming at designing artificial surfaces by mimicking them. Their results show that many biological surfaces, including leaves of water-repellent plants such as the lotus,[8] legs of insects such as the water strider,[9] feathers of animals such as pigeons,[10] and butterfly wings,[11] have a hierarchically structured surface roughness at two scale ranges: micro- and nanoscale roughness, which is optimized for superhydrophobicity through the natural selection.

With rapid improvements of micro-/nanofabrication techniques, it is now becoming possible to control and tailor micro-/

nanoscale chemical structures on solid surfaces. A key issue for fabricating a composite hierarchical structured surface is its stability. Many mimetic attempts have been made to manufacture industrially similar surfaces. For example, Wu et al.[12] have prepared double-walled carbon nanotube (DWCNT) macrofilms with large areas applying a floating catalyst CVD method using a solution of *n*-hexane and methanol as the carbon source. This large CNT film, showing excellent antifouling, self-cleaning, and water-repellent functions, can be bended or folded without any damage and even can be tailored freely. Jeong et al.[13] have presented a simple and yet robust method for fabricating well-defined micro-/nanoscale hierarchical structures using a two-step temperature-directed capillary molding process. Kwon et al.[14] have designed and fabricated an extreme water-repellent surface with a hierarchical integration of nano- and microscale textures by combining the two readily accessible etching techniques: a standard deep silicon etching and a gas-phase isotropic etching (XeF_2).

Accordingly, there have also been a few theoretical attempts toward the prediction of wetting behavior of dual-scale roughness surfaces. For example, Onda et al.[15] have studied the wettability of fractal surfaces theoretically. Results show that the

contact angle (CA) of a liquid droplet placed on a fractal surface can be expressed as a function of the fractal dimension, the range of fractal behavior, and the contacting ratio of the surface. Sajadinia et al.[16] found that the wettability of each component in dual-scale roughness structure may depend on the presence and geometrical parameters of other components. Bhushan et al.[17] demonstrate that hierarchical roughness makes super-hydrophobic states stable because a multiscale (hierarchical) roughness can effectively resist these scale-dependent mechanisms; THAT IS, the CA is scale dependent, which has been experimentally[18] verified. They also indicate that the high asperities resist the capillary waves, while nanobumps prevent nanodroplets from filling the valleys between asperities and pin the triple line in case of a hydrophilic spot.

However, to date, the comprehensive studies on the effects of different geometrical parameters for a multiscale of hierarchical structure on its wettability are still lack. In particular, there are hardly any theoretical studies to investigate quantitatively the thermodynamic mechanisms for the unique role of such hierarchical structures in superhydrophobic behavior.

In our previous paper,[19] we conducted a simple qualitative explanation on the effect of the hierarchical structures based on the proposed fundamental principles[20] for achieving superhydrophobic surfaces. In the present work, we conduct a systematic thermodynamic analysis in detail on free energy (FE) and free energy barrier (FEB), which determine thermodynamically the wettability, such as CA and contact angle hysteresis (CAH) as well as composite state. Using completely quantitative results, we try to understand completely the role of the hierarchical structures of natural superhydrophobic surfaces.

2. THERMODYNAMIC ANALYSIS

2.1. Wetting Theories on Rough Surfaces. The CA of a water droplet on an ideal smooth solid surface can be given by the classical Young's equation:

$$\gamma^{la} \cos \vartheta_Y = \gamma^{sa} - \gamma^{ls} \tag{1}$$

where ϑ_Y is Young's CA, that is, intrinsic CA; γ^{la}, γ^{sa}, and γ^{ls} are the surface tension at liquid—air, solid—air, and liquid—solid interfaces, respectively. When it comes to a rough surface, there are two models: complete liquid penetration into the troughs of a rough surface, which is called noncomposite wetting state, and the entrapment of air in the troughs of a rough surface, which is called composite state. The apparent CA of the noncomposite state is given by Wenzel's equation:[21]

$$\cos \vartheta_W = r \cos \vartheta_Y \tag{2}$$

where r is the roughness ratio between the actual area and geometric projected area for a wetting surface for the 2-D model.

Note that the surface microtexture is uniformly constructed from the constant geometrical parameters of pillar width (a), spacing (b), and height (h). Subscripts 1, 2, and 3 represent micropillars, submicropillars, and nanopillars, respectively. To mimic the self-similar structures in the nature, we consider that micropillar, submicropillar, and nanopillar have the same geometrical parameter ratios, that is, $a_1:b_1:h_1 \equiv a_2:b_2:h_2 \equiv a_3:b_3:h_3$. We use $a:b:h$ instead of the same geometrical parameter ratios, that is, $a_1:b_1:h_1$, $a_2:b_2:h_2$, and $a_3:b_3:h_3$. For the single-, dual-, and three-scale roughness pillar texture structures (see Figure 1), r, which is the value of roughness ratio of the overall surface, can be
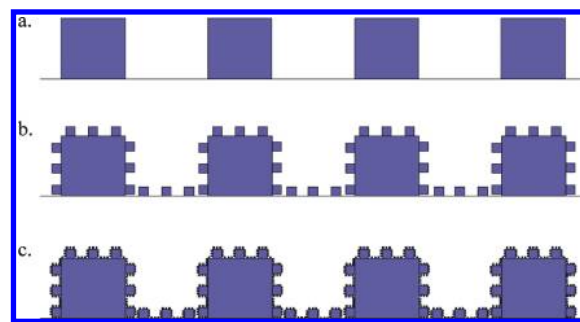

Figure 1. 2-D pillar texture structures of (a) single-, (b) dual-, and (c) three-scale roughness.

written as:

$$r = 1 + \frac{2h_1}{a_1 + b_1} \tag{3}$$

$$r = 1 + \frac{2h_2}{a_2 + b_2} \tag{4}$$

$$r = 1 + \frac{2h_3}{a_3 + b_3} \tag{5}$$

where n_1 and n_2 are the number of subpillars on the top of a micropillar and the number of nanopillars on the top of a submicropillar, respectively. They can be written as:

$$n_1 = \frac{a_1}{a_2 + b_2} \tag{6}$$

$$n_2 = \frac{a_2}{a_3 + b_3} \tag{7}$$

The apparent CA for the composite can be calculated using Cassie's equation:[22]

$$\cos \vartheta_C = f_s \cos \vartheta_Y + f_s - 1 \tag{8}$$

where f_s is the solid—liquid contact area fraction of the substrate for the 2-D model. For the single-, dual-, and three- scale roughness 2-D pillar texture structures, f_s can be written as:

$$f_s = \frac{a_1}{a_1 + b_1} = \frac{a}{a + b} \tag{9}$$

$$f_s = \frac{n_1 a_2}{a_1 + b_1} = \frac{a_1}{a_2 + b_2} \times \frac{a_2}{a_1 + b_1} = \left(\frac{a}{a + b}\right)^2 \tag{10}$$

$$f_s = \frac{n_1 n_2 a_3}{a_1 + b_1} = \frac{a_1}{a_2 + b_2} \times \frac{a_2}{a_3 + b_3} \times \frac{a_3}{a_1 + b_1}$$

$$= \left(\frac{a}{a + b}\right)^3 \tag{11}$$

Here, it is noted that for a given geometrical system, the value of roughness ratio does not change for the structures with different scales roughness, but f_s decreases as the scale of the structures increase.

2.2. Thermodynamic Analysis for Single-Scale (Micro-, Submicro-) and Hierarchical (Dual- and Three-Scale Roughness) Structures. In our previous study,[23] a FE analysis and
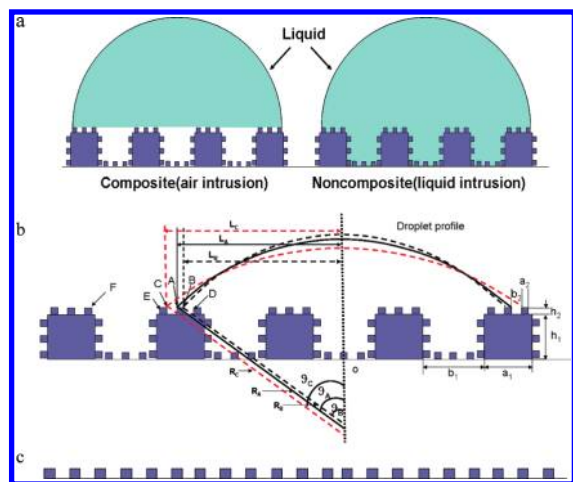
Figure 2. (a) Noncomposite and composite wetting states; (b) geometrical parameters and the movements of a drop; and (c) the equivalent structure for the noncomposite wetting state.

formulation was presented for a surface with the texture shown in Figure 1. To illustrate Figure 1 clearly, dual-roughness structure has a geometry of square micropillars with a size of $a_1 \times a_1$, height h_1, and spacing b_1 arranged regularly, which has submicropillars with a size of $a_2 \times a_2$, height h_2, and spacing b_2 arranged regularly on every side of the micropillars (a_1 and h_1) and the space between them (b_1). Here, we note that the space of submicropillars on the top and the side of micropillars is b_2; that is, the submicropillars are regularly arranged along $a_1 + h_1 + b_1$ in the 2-D structures. It is worth pointing out that we make minor adjustments of pillar space in the corner to avoid the occurrence of overleaping pillars in the corner. The formulation allows study of both noncomposite and composite wetting states. On the basis of the developed model, the thermodynamic analysis of the wetting states related to the surface texture geometry and numerical calculations of FE and FEB can be conducted. The effect of the single-roughness was discussed in our previous study. Here, we conduct thermodynamic calculations of hierarchical structures (such as dual-scale roughness structure shown in Figure 1b).

For the analysis of the 2D wetting system, we briefly mention the following assumptions, which have been explained clearly in the literature.[23]

(1) The droplet is small about at millimeter scale and is large enough as compared to the dimension of surface asperities. Thus, the gravity and the line tension, that is, the excess free energy of a solid—liquid—air system per unit length of the three-phase contact line, can be neglected.

(2) Chemical heterogeneity and interactions between water and solid and between fluidic molecules within droplet and molecules within solid can be ignored.

(3) The Young's equation is locally valid.

(4) On the basis of the above assumptions, the droplet is spherical in the absence of gravity, and liquid volume conservation can be kept. Thus, in the present 2-D model shown in Figure 1c, the droplet area should be constant.

Because of the similarity of the structure, a droplet is contacting either the tops of asperities or the bottoms of the troughs; middle status cannot occur.[23] Here, we should point out that this is different from the analysis of Liu et al.[24] and Seyed Hosein Sajadinia et al.[16] because of different characters of pillars.

For the simplicity, we can consider the situation for the non-composite wetting state of the dual structure (see Figure 2 a) to be equivalent to that of the single structure (see Figure 2 c). Thus:

$$F_{\text{non/dual}} = \gamma^{\text{la}} l_{\text{dual}}{}^{\text{la}} + C_1 \qquad (12)$$

$$F_{\text{non/single}} = \gamma^{\text{la}} l_{\text{single}}{}^{\text{la}} + C_1 \qquad (13)$$

where C_1 is the FE of the portion of the system that remains unchanged as a result of the substitute of noncomposite states of single structure for dual structure. For the given structure, we can derive the following relationships:

$$l_{\text{dual}}{}^{\text{la}} = \vartheta_0 R_0 = \frac{\vartheta_0 L_0}{\sin \vartheta_0} \qquad (14)$$

$$l_{\text{single}}{}^{\text{la}} = \vartheta_1 R_1 = \frac{\vartheta_1 L_1}{\sin \vartheta_1} \qquad (15)$$

$$L_1 = L_0 + \frac{L_0}{(a_1 + b_1)} \times 2h_1 \qquad (16)$$

According to the constant drop volume constraint or its 2D equivalent, we can derive the following:

$$\vartheta_0 \frac{L_0^2}{\sin^2 \vartheta_0} - L_0^2 ctg\vartheta_0 +$$
$$\frac{2L_0}{a_1 + b_1}\left[(a_1 + b_1)(h_1 + h_2) - a_2 h_2 \times \frac{a_1 + b_1 + 2h_1}{a_2 + b_2}\right]$$
$$= \vartheta_1 \frac{L_1^2}{\sin^2 \vartheta_1} - L_1^2 ctg\vartheta_1 + \frac{L_1}{a_2 + b_2} \times 2b_2 h_2 \qquad (17)$$

The FE change for substitute can be expressed as:

$$\frac{\Delta F_{\text{dual} \to \text{single}}}{\gamma^{\text{la}}} = \vartheta_1 \frac{L_1}{\sin \vartheta_1} - \vartheta_0 \frac{L_0}{\sin \vartheta_0} \qquad (18)$$

For the noncomposite of the single structure, if the drop recedes from position A with a CA (ϑ_A) to B with ϑ_B (Figure 2b), the magnitude of FE per unit length of drop perpendicular to $y = 0$ plane (F) for each of the two cases is represented as:

$$F_A = \gamma^{\text{la}} l_A{}^{\text{la}} + \gamma^{\text{ls}} l_A{}^{\text{ls}} + C_2 \qquad (19)$$

$$F_B = \gamma^{\text{la}} l_B{}^{\text{la}} + \gamma^{\text{sa}} l_B{}^{\text{sa}} + C_2 \qquad (20)$$

where C_2 is the FE of the portion of the system that remains unchanged as a result of receding; $l_A{}^{\text{la}} = \vartheta_1 R_1 = \vartheta_1 L_1/\sin \vartheta_1$ and $l_A{}^{\text{ls}} = l_B{}^{\text{sa}} = a_2$, where R_1 is radius of curvature of the drop, L_1 is drop width, and a_2 is pillar width of a submicropillar in the plane of analysis.

Resulting from assumption (4), the geometrical equation can be expressed as:

$$\vartheta_A \frac{L_A^2}{\sin^2 \vartheta_A} - L_A^2 ctg\vartheta_A = \vartheta_B \frac{L_B^2}{\sin^2 \vartheta_B} - L_B^2 ctg\vartheta_B \qquad (21)$$

The change of FE (i.e., FEB) from A to B can be written as:

$$\frac{\Delta F_{A \to B}}{\gamma^{\text{la}}} = \left(\vartheta_B \frac{L_B}{\sin \vartheta_B} - \vartheta_A \frac{L_A}{\sin \vartheta_A}\right) + a_2 \cos \vartheta_Y \qquad (22)$$

If the drop advances from A to C and from E to F (see Figure 2c), there will be a similar FE barrier; the difference is leaping over
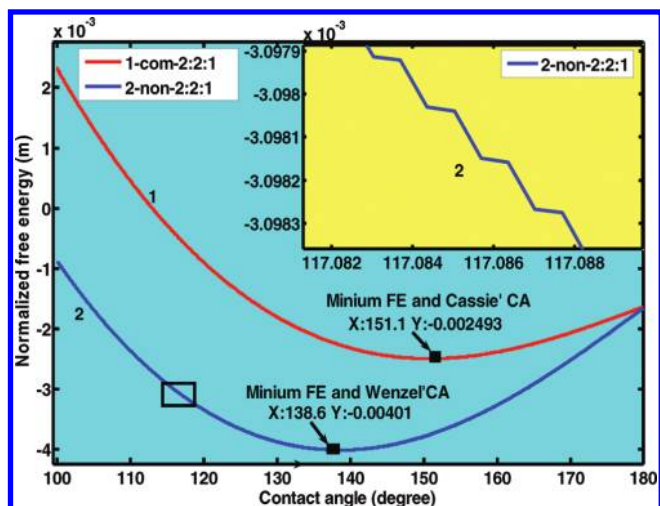
Figure 3. Variation of normalized FE with CA of both wetting states for the dual structure ($L = 10^{-2}$ m, $a_1 = b_1 = 2h_1 = 2 \times 10^{-5}$ m, $a_2 = b_2 = 2h_2 = 2 \times 10^{-7}$ m, intrinsic CA, $\vartheta_Y = 120°$).

different spacing. Also, it can be calculated in a similar fashion:

$$\vartheta_A \frac{L_A^2}{\sin^2 \vartheta_A} - L_A^2 ctg\vartheta_A = \vartheta_C \frac{L_C^2}{\sin^2 \vartheta_C} - L_C^2 ctg\vartheta_C + 2b_2h_2 \tag{23}$$

$$\frac{\Delta F_{A \to C}}{\gamma^{la}} = \left(\vartheta_C \frac{L_C}{\sin \vartheta_C} - \vartheta_A \frac{L_A}{\sin \vartheta_A} \right) - (2h_2 + b_2) \cos \vartheta_Y \tag{24}$$

Therefore, similarly, for the composite state (see Figure 2a):

$$\vartheta_A \frac{L_A^2}{\sin^2 \vartheta_A} - L_A^2 ctg\vartheta_A = \vartheta_B \frac{L_B^2}{\sin^2 \vartheta_B} - L_B^2 ctg\vartheta_B \tag{25}$$

$$\frac{\Delta F_{A \to B}}{\gamma^{la}} = \left(\vartheta_B \frac{L_B}{\sin \vartheta_B} - \vartheta_A \frac{L_A}{\sin \vartheta_A} \right) + a_2 \cos \vartheta_Y \tag{26}$$

$$\vartheta_A \frac{L_A^2}{\sin^2 \vartheta_A} - L_A^2 ctg\vartheta_A = \vartheta_C \frac{L_C^2}{\sin^2 \vartheta_C} - L_C^2 ctg\vartheta_C \tag{27}$$

$$\frac{\Delta F_{A \to C}}{\gamma^{la}} = \left(\vartheta_C \frac{L_C}{\sin \vartheta_C} - \vartheta_A \frac{L_A}{\sin \vartheta_A} \right) + b_2 \tag{28}$$

$$\vartheta_E \frac{L_E^2}{\sin^2 \vartheta_E} - L_E^2 ctg\vartheta_E = \vartheta_F \frac{L_F^2}{\sin^2 \vartheta_F} - L_F^2 ctg\vartheta_F \tag{29}$$

$$\frac{\Delta F_{E \to F}}{\gamma^{la}} = \left(\vartheta_F \frac{L_F}{\sin \vartheta_F} - \vartheta_E \frac{L_E}{\sin \vartheta_E} \right) + b_1 \tag{30}$$

A reference FE state is assigned as a value of zero by a random choice (e.g., the instantaneous position A) with the initial drop size L_0 and contact angle ϑ_0, respectively. Hence, the reference state cannot affect the results of FEB, which is a relative value with respect to its neighbors (e.g., B and C). The FEB such as $\Delta F_{A \to B}$ and $\Delta F_{A \to C}$ can be determined by the numerical computations. Similarly, geometrical constraint and FEB equations for other arbitrary instantaneous positions can also be derived.
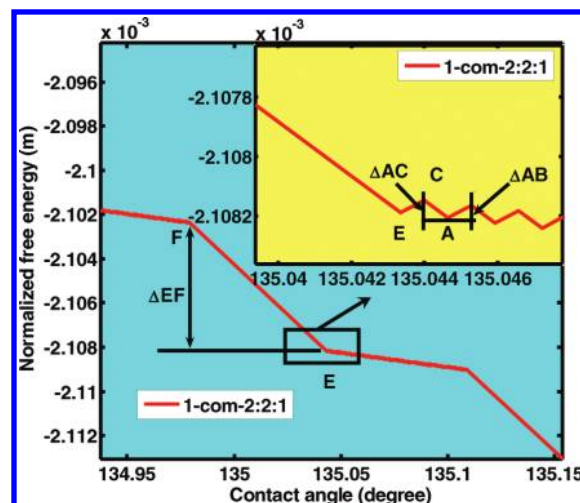

Figure 4. The enlarged FE curves of the composite wetting state shown in Figure 3. Positions A, B, C, D, E, and F correspond to those in Figure 2b. ΔAB represents the FEB for retreating contact line; ΔAC and ΔEF represent the FEBs for advancing contact lines.

A similar method is used for the three-scale roughness structure.

3. RESULTS AND DISCUSSION

3.1. Typical FE and FEB Curves. For various ϑ values representing the range of possible CA between advancing and receding, using eqs 21−30, the change in FE or the FE barrier can be calculated.

Figure 3 shows typical both noncomposite (non) and composite (com) FEs variation with respect to CA for the dual-scale roughness microstructure ($L = 10^{-2}$ m, $a_1 = b_1 = 2h_1 = 2 \times 10^{-5}$ m, $a_2 = b_2 = 2h_2 = 2 \times 10^{-7}$ m; intrinsic CA, i.e., $\vartheta_Y = 120°$). Note that, as described, FE (J/m) is normalized with respect to γ (J/m²), and the unit of FE will then be meters. There is only one point of the lowest FE for the composite FE curve, that is, the global lowest point, which is associated with the equilibrium CA (ECA) and represents the stable equilibrium state. From the inset in Figure 3 for the noncomposite system, we can see that there are first-level fluctuations in FE after enlarging, which is different from the composite system because of equivalent structure as explained above.

Figure 4 shows the composite FE curve and different enlarging segments. One can see that the local curve can show first-level fluctuations in FE after enlarging (see points E and F). This indicates that the FE curve contains multivalued local minimum and maximum FE, representing metastable (e.g., point E) and unstable (e.g., point F) equilibrium states, respectively, because of the existence of micropillars on the smooth surface. After further enlarging a part of the curve shown in the inset, there are other multivalued local minimum and maximum FE, that is, second-level fluctuations, representing submetastable (e.g., points A and D) and unstable (e.g., points B and C) equilibrium states, respectively. This is because of the existence of submicro pillars on the microstructure pillar.

Here, we can see that there are two orders of advancing FEB. For example, ΔEF illustrated in Figure 4 is on the order of micropillar's advancing FEB, representing the advancing FEB when the droplet advances from the edge of one submicropillar
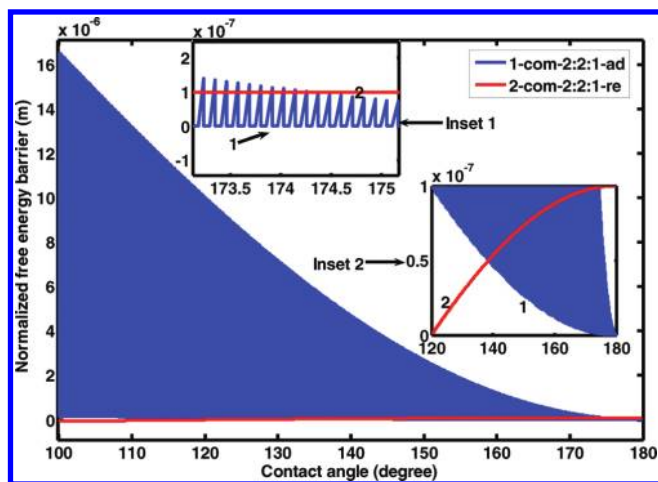
Figure 5. Typical curves of advancing and receding FEBs of a composite wetting state for the dual structure ($L = 10^{-2}$ m, $a_1 = b_1 = 2h_1 = 2 \times 10^{-5}$ m, $a_2 = b_2 = 2h_2 = 2 \times 10^{-7}$ m, intrinsic CA, $\vartheta_Y = 120°$).
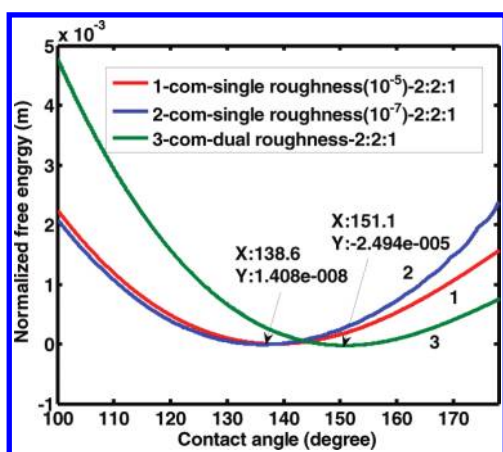

Figure 6. Variation of normalized FE with CA of a composite wetting state for single- and dual-scale roughness structures ($L = 10^{-2}$ m, $a_1 = b_1 = 2h_1 = 2 \times 10^{-5}$ m, $a_2 = b_2 = 2h_2 = 2 \times 10^{-7}$ m, intrinsic CA, $\vartheta_Y = 120°$).
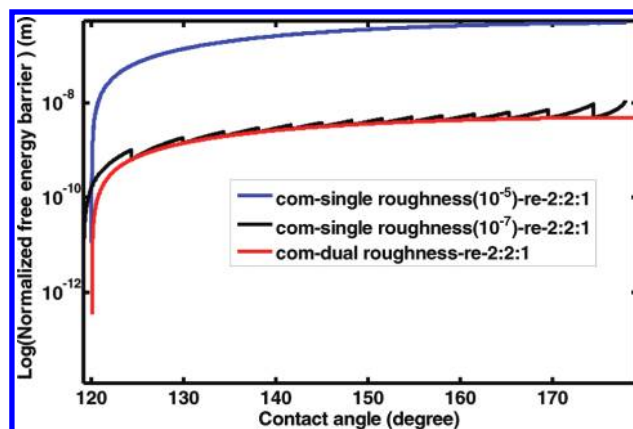

Figure 7. Receding FEB curves of the composite wetting state for single- and dual-scale roughness structures ($L = 10^{-2}$ m, $a_1 = b_1 = 2h_1 = 2 \times 10^{-5}$ m, $a_2 = b_2 = 2h_2 = 2 \times 10^{-7}$ m, intrinsic CA, $\vartheta_Y = 120°$).
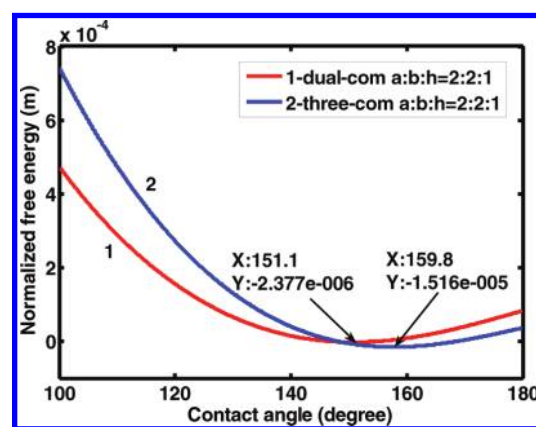

Figure 8. Variation of normalized FE with CA for composite wetting states of dual- and three-scale roughness structures ($L = 10^{-2}$ m, $a_1 = b_1 = 2h_1 = 2 \times 10^{-5}$ m, $a_2 = b_2 = 2h_2 = 2 \times 10^{-7}$ m, $a_3 = b_3 = 2h_3 = 2 \times 10^{-9}$ m, intrinsic CA, $\vartheta_Y = 120°$).

above one micropillar to the one above the next micropillar (e.g., from E to F) in the direction of three-phase motion, and ΔAC illustrated in the inset is on the order of submicropillar's advancing FEB, representing the advancing FEB when the droplet advances from the edge of one submicropillar above one micropillar to the adjacent one above the same micropillar (e.g., from A to C) in the direction of three-phase motion. The difference between ΔEF and ΔAC is significant differences between the sizes. We also find that there is only one order of receding FEB, that is, the order of submicropillar's receding FEB. For example, ΔAB illustrated in the inset is the receding FEB when droplet recedes from the edge of one submicropillar to the adjacent one in the direction of three-phase motion.

Similarly, we can explain the differences of FEBs for the dual-scale roughness topography. Because of submicropillars onto every micropillar, for advancing, a droplet reaps two kinds of pillar spacing: submicropillar spacing (b_2) and micropillar spacing (b_1); however, for receding, the droplet moves just along the submicropillar one edge to the other edge, that is, the same submicropillar spacing (b_2).

Therefore, as compared to the advancing curve of the single-scale roughness pillar structure, the advancing FEB curve in Figure 5 is no longer smooth. It fluctuates between micro- and submicro-order advancing FEBs. Also, the receding curve shown in Figure 7 is similar to the one of the single-scale roughness pillar structure. From the comparison of the two receding curves, one can see that the receding curve becomes much lower than the one of single-scale roughness pillar structure.

3.2. The Effects of Hierarchical Structure. *3.2.1. The Effects of Hierarchical Structure on ECA.* Figure 6 illustrates comparisons of variations of normalized FE with apparent CA for composite (com) wetting systems of micro-, submicro-, and dual-scale roughness structures ($L = 10^{-2}$ m, $a:b:h = 2:2:1$; for dual-scale roughness structure, $a_1 = b_1 = 2h_1 = 2 \times 10^{-5}$ m, $b_2 = 2h_2 = 2 \times 10^{-7}$ m; for micro-scale roughness structure, $a_1 = b_1 = 2h_1 = 2 \times 10^{-5}$ m; for submicro-scale roughness structure, $a_2 = b_2 = 2h_2 = 2 \times 10^{-7}$ m; intrinsic CA, $\theta_Y = 120°$).

The calculated results show that the dual-scale roughness structure hardly has any change in FE but can lead to a larger ECA for the same geometrical parameters ratio. From Figure 6, we can also see clearly that Cassie's CAs for the composite of micro-, submicro-, and dual-scale roughness structures are
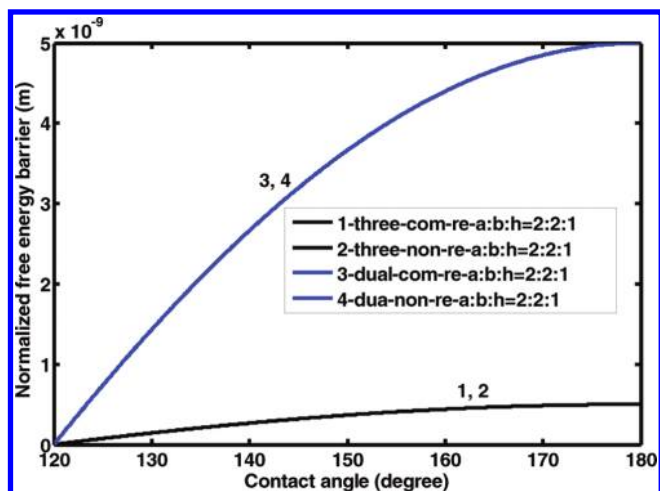
Figure 9. Receding FEB curves for both wetting states of dual- and three-scale roughness structures ($L = 10^{-2}$ m, $a_1 = b_1 = 2h_1 = 2 \times 10^{-5}$ m, $a_2 = b_2 = 2h_2 = 2 \times 10^{-7}$ m, $a_3 = b_3 = 2h_3 = 2 \times 10^{-9}$ m, intrinsic CA, $\vartheta_Y = 120°$).

Figure 10. Comparison of variations of normalized FE with apparent CA of both wetting states for dual structures with different relative pillar heights ($L = 10^{-2}$ m, $a_1 = b_1 = 2 \times 10^{-5}$ m, $a_2 = b_2 = 2 \times 10^{-7}$ m, intrinsic CA, $\vartheta_Y = 120°$).

calculated to be ϑ_C = 138.6°, 138.6°, and 151.1°, respectively; these exactly correspond to the CAs with the minimum FE found from Figure 6. Therefore, if the ratio is the same, dual-scale roughness structure can provide a much larger ECA.

Furthermore, on the basis of the comparison of FE for the composite system between the dual- and three-scale roughness structures in Figure 8, one can see that the ECA for three-scale roughness structure (i.e., 159.8°) is larger than that of the dual-scale roughness structure (i.e., 151.1°). This indicates that the three-scale roughness structure can provide the largest ECA for the same ratio.

3.2.2. The Effects of Hierarchical Structure on FEB. Figure 7 shows variations of the normalized receding FE barrier with apparent CAs of the micro-, submicro-, and dual-structures for composite wetting system. One can see that all of the receding curves cross the *x*-axis at the CA of 120°. This implies that the hierarchical structure does not affect the receding CA for composite wetting system. This happens because the vibrational energy is assumed as zero in the present study. Here, we point out that if the vibrational energy is not zero, the receding CA depends strongly on the surface patterns.

The calculated results also show that both dual- and submicro-scale (single-scale) roughness structures can decrease receding FE barriers. In addition, from the comparison of the receding FE barriers for the three-scale and dual-scale roughness structures (see Figure 9) for the same geometrical parameters ratio, one can see that the receding FEB of the three-scale roughness structure (on the order of 10^{-10} m) is much lower than that of the dual-scale roughness structure (on the order of 10^{-9} m). Such a low FEB means that if the wetting system gains a slight external energy, the receding CA can increase greatly. This therefore indicates a simple strategy for reducing or eliminating CAH, which has been supported experimentally by Gao et al.[25]

3.3. The Effects of Geometrical Parameter Ratio. *3.3.1. The Effect of Relative Trough Height h_r (h/b) on ECA and FEB.* Figure 10 illustrates the variations of FE with respect to CA for both noncomposite and composite wetting states for different relative trough height h_r (h/b). From the figure, one can see that when h_r is the critical relative trough height, h_{rc} (for the geometrical conditions in Figure 10, h_{rc} = 0.75), both composite and

Figure 11. Curves of advancing and receding FEBs of both wetting states for dual structures with different relative pillar heights ($L = 10^{-2}$ m, $a_1 = b_1 = 2 \times 10^{-5}$ m, $a_2 = b_2 = 2 \times 10^{-7}$ m, intrinsic CA, $\vartheta_Y = 120°$).

noncomposite wetting state FEs curves overlap; when h_r is smaller than 0.75, the FE of composite wetting state is higher than that of noncomposite wetting state; when h_r is larger than 0.75, the FE of composite wetting state is lower than that of noncomposite wetting state. This means that the composite
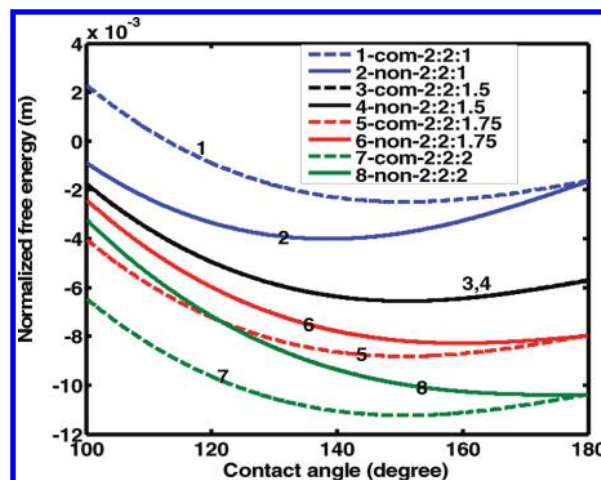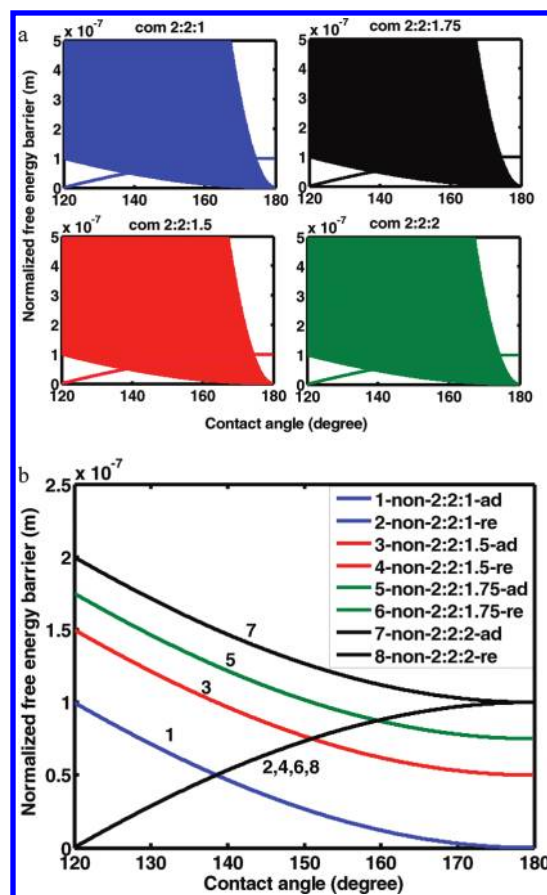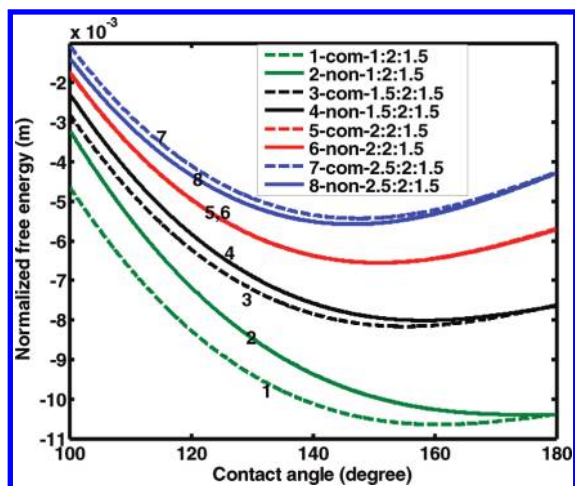
Figure 12. Comparison of variations of normalized FE with apparent CA of both wetting states for dual structures with different relative pillar widths ($L = 10^{-2}$ m, $b_1 = 4/3h_1 = 2 \times 10^{-5}$ m, $b_2 = 4/3h_2 = 2 \times 10^{-9}$ m, intrinsic CA, $\vartheta_Y = 120°$).
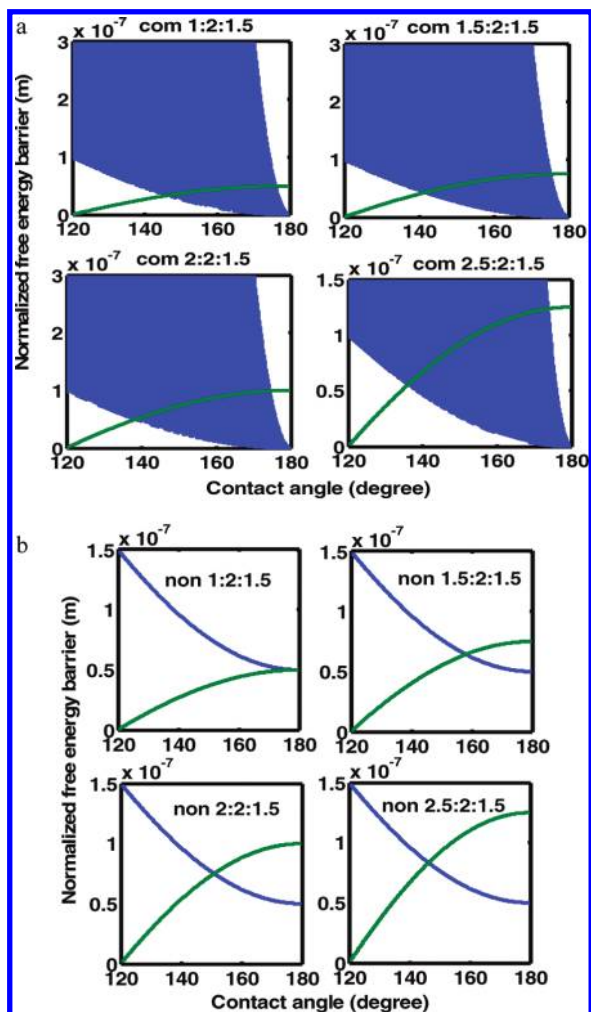

Figure 13. Curves of advancing and receding FEBs of both wetting states for dual structures with different relative pillar widths ($b_1 = 4/3h_1 = 2 \times 10^{-5}$ m, $b_2 = 4/3h_2 = 2 \times 10^{-9}$ m, $L = 10^{-2}$ m, intrinsic CA, $\vartheta_Y = 120°$).
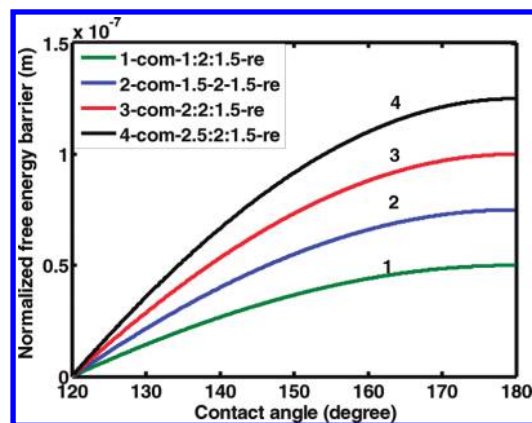

Figure 14. Comparison of receding FEB curves of the composite wetting state for dual structures with different relative pillar widths ($b_1 = 4/3h_1 = 2 \times 10^{-5}$ m, $b_2 = 4/3h_2 = 2 \times 10^{-9}$ m, $L = 10^{-2}$ m, intrinsic CA, $\vartheta_Y = 120°$).

wetting state is more stable than the noncomposite wetting state as h_r increases, indicating that larger h_r can lead to a more stable composite wetting state.

Figure 11 illustrates the effects of relative trough height on FEBs for both noncomposite and composite wetting systems. One can see that all of the receding FEB curves of noncomposite and composite wetting states with different relative pillar heights overleap. This means that the receding FEB curves both of noncomposite and composite wetting states do not depend on the relative trough height. Figure 11 also shows that the advancing FEBs of composite wetting state are basically unchanged with the different relative trough height, while for the noncomposite wetting state, the advancing FEBs decrease sharply as h_r decreases.

3.3.2. The Effect of Relative Pillar Width a_r (a/b) on ECA and FEB. Figure 12 illustrates variations of normalized FE with apparent CA between noncomposite and composite wetting states for different relative pillar widths. One can see that there exists a critical relative pillar width ($a_{rc} = 1$).

Figure 13 illustrates the FEBs of both wetting systems for different relative pillar widths. One can see that the advancing FEBs of composite wetting state remain unchanged, indicating that relative pillar width has no effects on the advancing FEBs. However, from comparisons of receding FEBs for both non-composite and composite states (see Figure 13b) of the dual-scale roughness structure (see Figure 14), one can see that the receding FEB decreases with a decrease in a_r. This means that we can simply decrease CAH by increasing the vibrational energy slightly, for example, on the order of 10^{-9} m.

4. CONCLUSIONS

On the basis of a proposed thermodynamic approach, different scales of hierarchical structures have been theoretically investigated. The effect of surface geometries of the single-, dual-, and three-scale roughness on FE and FEB as well as CA and CAH is discussed in detail. If the geometrical parameter ratio is the same (e.g., $a:b:h = 2:2:1$), for the composite state, the ECA of the three-, dual-, and single-scale roughness structures is 159.8°, 151.1°, and 138.6°, respectively. Furthermore, for FE curves, there is a first-level fluctuation (i.e., FEB) for the single-scale roughness structure, first-level and second-level fluctuations

for the dual-scale roughness structure, and first-level, second-level, and third-level fluctuations for the three-scale roughness structure. Such fluctuations can split a large FEB into many small ones and hence can decrease receding FEB, which is especially helpful to improve the so-called self-cleaning property. In addition, for extremely small droplets, the primary structure (i.e., microstructure) may fail to keep the composite wetting state, whereas the secondary or third structure (i.e., submicrostructure or nanostructure) can play a dominant role in resisting the droplets into troughs of the rough structures.

In summary, the three-scale roughness structure with a large h_r and a small a_r can lead to the stable composite wetting state, large ECA, and small CAH (especially for a slight external energy) as well as good mechanical durability.

■ AUTHOR INFORMATION

Corresponding Author
*E-mail: wenl@ualberta.ca.

■ ACKNOWLEDGMENT

■ REFERENCES

(1) Mandelbrot, B.; Abhyankar, P. C. a. S. *Math. Intell.* **1977**, *1*, 35–37.

(2) Mandelbrot, B. *Science* **1967**, 155.

(3) Mandelbrot, B. *Math. Intell.* **1982**, 1.

(4) Guo, Z.; Liu, W.; Su, B.-L. *Appl. Phys. Lett.* **2008**, *93*, 201909–3.

(5) Bharat, B.; Yong Chae, J. *J. Phys.: Condens. Matter* **2008**, *20*, 225010.

(6) Bhushan, B.; Jung, Y. C.; Koch, K. *Philos Trans. R. Soc., A* **2009**, *367*, 1631–1672.

(7) Bhushan, B.; Jung, Y. C. *Prog. Mater. Sci.* **2010** in press.

(8) Wang, J.; Chen, H.; Sui, T.; Li, A.; Chen, D. *Plant Sci.* **2009**, *176*, 687–695.

(9) Feng, X.-Q.; Gao, X.; Wu, Z.; Jiang, L.; Zheng, Q.-S. *Langmuir* **2007**, *23*, 4892–4896.

(10) Bormashenko, E.; Bormashenko, Y.; Stein, T.; Whyman, G.; Bormashenko, E. *J. Colloid Interface Sci.* **2007**, *311*, 212–216.

(11) Fang, Y.; Sun, G.; Wang, T.; Cong, Q.; Ren, L. *Chin. Sci. Bull.* **2007**, *52*, 711–716.

(12) Wu, Z.; Xu, Q.; Wang, J.; Ma, J. *J. Mater. Sci. Technol.* **2010**, *26*, 20–26.

(13) Jeong, H. E.; Lee, S. H.; Kim, J. K.; Suh, K. Y. *Langmuir* **2006**, *22*, 1640–1645.

(14) Kwon, Y.; Patankar, N.; Choi, J.; Lee, J. *Langmuir* **2009**, *25*, 6129–6136.

(15) Onda, T.; Shibuichi, S.; Satoh, N.; Tsujii, K. *Langmuir* **1996**, *12*, 2125–2127.

(16) Sajadinia, S. H.; Sharif, F. *J. Colloid Interface Sci.* **2010**, *344*, 575–583.

(17) Michael, N.; Bhushan, B. *Microelectron. Eng.* **2007**, *84*, 382–386.

(18) Cheng, Y.-T. *Appl. Phys. Lett.* **2005**, *87*, 194112.

(19) Li, W.; Amirfazli, A. *Soft Matter* **2007**, *4*, 462–466.

(20) Li, W.; Amirfazli, A. *Adv. Colloid Interface Sci.* **2007**, *132*, 51–68.

(21) Wenzel, R. N. *Ind. Eng. Chem.* **1936**, *28*, 988–994.

(22) Cassie, A. B. D.; Baxter, S. *Trans. Faraday Soc.* **1944**, *40*, 546–51.

(23) Li, W.; Amirfazli, A. *J. Colloid Interface Sci.* **2005**, *292*, 195–201.

(24) Liu, T.; Sun, W.; Sun, X.; Ai, H. *Langmuir* **2010**, *26*, 14835–14841.

(25) Gao, L.; McCarthy, T. J. *Langmuir* **2006**, *22*, 2966–2967.